

Satellites in the Ti 1s core level spectra of SrTiO₃ and TiO₂

Atsushi Hariki¹,[✉] Keisuke Higashi,¹ Tatsuya Yamaguchi,¹ Jiebin Li,² Curran Kalha,² Manfred Mascheck,³ Susanna K. Eriksson,⁴ Tomas Wiell,⁴ Frank M. F. de Groot,⁵ and Anna Regoutz^{2,*}

¹*Department of Physics and Electronics, Graduate School of Engineering,*


Osaka Metropolitan University, 1-1 Gakuen-cho, Nakaku, Sakai, Osaka 599-8531, Japan

²*Department of Chemistry, University College London, 20 Gordon Street, London WC1H 0AJ, United Kingdom*

³*Scienta Omicron GmbH, Limburger Strasse 75, 65232 Taunusstein, Germany*

⁴*Scienta Omicron AB, P.O. Box 15120, 750 15 Uppsala, Sweden*

⁵*Materials Chemistry & Catalysis, Debye Institute for Nanomaterials Science, Utrecht University, Universiteitsweg 99, 3584 CG, Utrecht, The Netherlands*

 (Received 20 June 2022; revised 11 October 2022; accepted 24 October 2022; published 23 November 2022)

Satellites in core level spectra of photoelectron spectroscopy (PES) can provide crucial information on the electronic structure and chemical bonding in materials, particularly in transition metal oxides. This paper explores satellites of the Ti 1s and 2p core level spectra of SrTiO₃ and TiO₂. Conventionally, soft x-ray PES (SXPS) probes the Ti 2p core level; however, it is not ideal to fully capture satellite features due to its inherent spin-orbit splitting (SOS). Here, hard x-ray PES (HAXPES) provides access to the Ti 1s spectrum instead, which allows us to study intrinsic charge responses upon core-hole creation without the complication from SOS and with favorable intrinsic linewidths. The experimental spectra are theoretically analyzed by two impurity models, including an Anderson impurity model (AIM) built on local density approximation (LDA) and dynamical mean-field theory (DMFT), and a conventional TiO₆ cluster model. The theoretical results emphasize the importance of explicit inclusion of higher-order Ti-O charge-transfer processes beyond the nearest-neighbor Ti-O bond to simulate the core level spectra of SrTiO₃ and TiO₂. The AIM approach with continuous bath orbitals provided by LDA+DMFT represents the experimental spectra well. Crucially, with the aid of the LDA+DMFT method, this paper provides a robust prescription of how to use the computationally cheap cluster model in fitting analyses of core level spectra.

DOI: [10.1103/PhysRevB.106.205138](https://doi.org/10.1103/PhysRevB.106.205138)

I. INTRODUCTION

Transition metal oxides (TMOs) display a rich variety of functional properties, such as high-temperature superconductivity and colossal magnetoresistance [1,2], that have afforded them a high level of interest both fundamentally and in applications. Their properties emerge from atomic Coulomb multiplets embedded into their lattice, forming covalent bonds between transition metal (TM) and ligand orbitals. The nature of their electronic structure and chemical bonding is crucial to explain their functional properties, and photoelectron spectroscopy (PES) has been established as a powerful technique to directly probe both aspects of TMOs. Hard x-ray PES (HAXPES) has provided particularly useful insights regarding the bulk properties of these materials [3,4]. By going beyond the 2 keV maximum excitation energy of soft x-ray PES (SXPS), HAXPES increases the probing depth significantly, enabling the study of the bulk rather than the surface of a material. In the case of TiO₂, for example, the maximum inelastic mean free path, as calculated using the TPP-2M approach implemented in the QUASES software package [5], increases from 2.8 nm at the common soft x-ray excitation energy of 1.487 keV (Al K α) to 12.7 nm at the hard x-ray energy of 9.252 keV used in this paper.

In the case of 3d TMOs, the most widely studied core level using PES is the 2p state, which delivers rich information on their electronic structure, ranging from metal-insulator transitions to magnetic and orbital ordering [6–15]. This is possible, as the electronic response to the local perturbation (i.e., the creation of a core hole) gives rise to specific spectral features due to charge-transfer screening from surrounding ions via the underlying chemical bonding [7,8,16,17]. However, the analysis and interpretation of the already complex satellite structures present in the 2p state are further complicated by the presence of spin-orbit splitting (SOS) effects leading to overlap of spectral features within the core spectral range. Here, HAXPES brings an additional advantage over SXPS in providing access to deeper core states, which can be advantageous for spectral analysis due to absence of SOS, favorable intrinsic linewidths, reduction of overlap with other spectral features including core and Auger lines, and higher photo-ionization cross-sections [17–24]. This has already been exploited in the case of 3d TMOs, by accessing their 1s core states using HAXPES, particularly for the late TMOs [12,17,18,25,26].

Due to the complexity of the spectra, theoretical approaches to aid their interpretation are crucial. Since the core hole does not move and it couples exclusively to the localized *d* electrons on the same TM site, an impurity model representing the excited ion is a good starting point for modeling core

*a.regoutz@ucl.ac.uk

level spectra. For $3d$ TMOs, the MO_6 cluster model is widely employed [27,28]. It includes the x -ray excited metal and the surrounding ligands, thus implementing metal-oxygen (M–O) hybridization on the nearest-neighboring bond. Though the cluster model serves as a convenient platform for simulating spectra, it can suffer from a number of limitations: (1) hybridization between long-distance M–O and M–M bonds is lacking in the cluster model, which may be relevant for a charge response to the core hole, and (2) electronic configurations accompanied by higher-order electron exchange with the ligands, which are usually discarded to make the computation feasible, may affect the simulated spectra. Especially for highly covalent early TMOs, these limitations modify the model parameters during fitting of experimental data as well as impact the interpretation of spectral features.

This paper explores the Ti $1s$ and $2p$ core level spectra of SrTiO_3 and TiO_2 , prototype titanium oxides, using both experiment and theory. HAXPES is used to enable access to their Ti $1s$ spectra and bulk information on their electronic structure. Experimental results are fitted by two theoretical impurity models: (1) a TiO_6 cluster model and (2) an Anderson impurity model (AIM) built on local density approximation (LDA) combined with dynamical mean-field theory (DMFT) [8,17,29,30]. The latter can be viewed as an extension of the cluster model to incorporate hybridization among long-distance bonds while retaining the impurity model description. This is achieved by replacing the ligand orbitals in the cluster model by the continuous bath provided by LDA+DMFT, which represents an electron exchange with the distant ions in the periodic lattice. LDA+DMFT AIM has already been employed successfully to identify spectral features due to long-distance charge transfer in $2p$ and $1s$ x -ray photoelectron spectroscopy (XPS) spectra of mid- and late TMOs [8,17,31,32]. Here, this method is expanded to titanium oxides to examine the validity of the impurity model description for core level spectra of early TMOs, where covalency plays a crucial role.

II. METHOD

A. Experimental method

Two single crystals of rutile TiO_2 (110) and SrTiO_3 (100) were used for the measurements. The SrTiO_3 crystal was 1% doped with Nb to increase its conductivity. Both crystals were purchased from CRYSTAL, and no further sample preparation was needed. HAXPES measurements were performed on a Scienta Omicron HAXPES Lab system [33,34]. This spectrometer uses a monochromated Ga $K\alpha$ x -ray source, giving an excitation energy of 9.252 keV, and a Scienta Omicron EW4000 hemispherical electron energy analyzer to collect the excited photoelectrons. A pass energy of 200 eV, grazing incidence geometry ($<3^\circ$), and near-normal emission geometry were used for all measurements. The total energy resolution of this setup is 485 meV (16/84% width of the Au E_F). More details about the experimental setup can be found in a previous publication [33]. Complementary SXPS measurements were performed on a Thermo Scientific K-Alpha XPS system, which uses a monochromated Al $K\alpha$ x -ray source ($h\nu = 1.487$ keV). Measurements were conducted with a 400 μm

spot size, and a flood gun was used for charge compensation. Pass energies of 20 and 15 eV were used for core and valence spectra, respectively. The total energy resolution at 15 eV is 420 meV (16/84% width of the Au E_F).

B. Computational method

The Ti $1s$ HAXPES simulations start with a standard LDA+DMFT calculation [29,30,35]. The LDA bands obtained for the experimental structures of the studied compounds are projected onto a tight-binding model spanning Ti $3d$ and O $2p$ orbitals [36–38]. The tight-binding model was augmented with a local electron-electron interaction within the Ti $3d$ shell, defined by Hubbard U and Hund's J parameters with values of $(U, J) = (4.78$ eV, 0.64 eV), which are chosen by consulting with previous density functional theory (DFT)-based and spectroscopy studies for titanates including SrTiO_3 and TiO_2 [39–44].

The present LDA+DMFT implementation follows Refs. [8,17,32]. The strong-coupling continuous-time quantum Monte Carlo impurity solver [45–48] is used to compute the self-energies $\Sigma(i\omega_n)$ of Ti $3d$ electrons from the AIM. In the LDA+DMFT scheme, the bare energies of these d states are obtained from the LDA values by subtracting the so-called double-counting correction μ_{dc} , which accounts for the effect of the interaction already present in the LDA result [29,49]. Its appropriate value is determined by comparing the LDA+DMFT result with the experimental PES and the bandgap, as discussed below. All calculations are performed at $T = 300$ K. After converging the DMFT calculation, analytically continued $\Sigma(\varepsilon)$ in the real-frequency domain is obtained using the maximum entropy method [50]. It is then used to calculate the real-frequency one-particle spectral densities and hybridization densities $V^2(\varepsilon)$. The latter represents the exchange of electrons between the Ti ion and the rest of the crystal.

Ti $1s$ HAXPES spectra were computed from AIM with the DMFT hybridization densities $V^2(\varepsilon)$. AIM includes the Ti $1s$ core orbital and its Coulomb interaction with $3d$ electrons explicitly. The Coulomb interaction parameter between the $1s$ hole and Ti $3d$ electrons U_{dc} is set to $U_{dc} = 1.3 \times U_{dd}$, where U_{dd} is the configuration averaged Coulomb interaction between Ti $3d$ electrons, and the value is $U_{dd} = 4.5$ eV for the used Hubbard U and Hund's J values [17]. This is a well-established empirical rule in simulating core level XPS of $3d$ TMOs [8]. A configuration-interaction (CI) method for computing the HAXPES intensities is employed, for details see Refs. [8,51]. The CI scheme, which is widely used in computing the core level spectra using an impurity-based model, generates basis configurations by a sequential exchange of electrons between the impurity site and the bath (representing the rest of the crystal) starting with a normal-valence configuration, i.e., $|d^0\rangle$ for tetravalent Ti systems. The initial state $|g\rangle$ is described by a linear combination of the configurations as

$$|g\rangle = |d^0\rangle + |d^1\bar{L}\rangle + |d^2\bar{L}^2\rangle + |d^3\bar{L}^3\rangle + |d^4\bar{L}^4\rangle + \dots$$

Here, \bar{L} denotes a hole in the valence orbitals of the bath, and thus, $|d^n\bar{L}^m\rangle$ represents an electronic configuration with n d -electrons in the impurity Ti site and m holes in the valence bands. Ti $1s$ HAXPES final states are then described by

the configurations above plus a core hole in the Ti 1s shell. Spectra calculated by the conventional TiO_6 cluster model are also presented. Though the cluster model implements the same intra-atomic interactions as the LDA+DMFT AIM, the valence orbitals consist of only the 2p orbitals on the nearest-neighbor ligands. The hybridization strength between the Ti 3d and O 2p orbitals of the cluster model is extracted from the tight-binding model construed above, and the values are provided below. Though the CI scheme provides a systematic way to include the hybridization effect starting from the isolated atomic limit ($|d^0\rangle$), care may need to be taken for the cutoff in the basis expansion above, which will be discussed below.

In previous studies for Ti 2p, 3s, and 3p core level XPS spectra of Ti oxides using the TiO_6 cluster model [39,52], three electronic configurations ($|d^0\rangle$, $|d^1\underline{L}\rangle$, and $|d^2\underline{L}^2\rangle$) are considered in the spectral analysis.

To enable a direct comparison between the theoretically obtained projected density of states (PDOS) and the experimental valence band spectra, the PDOS results were broadened and photo-ionization cross-section corrected. Broadening and cross-sections were chosen to match the Al $K\alpha$ SXPS measurements, including a Gaussian broadening of 420 meV commensurate with the total energy resolution of the experiment and Scofield cross-sections [53,54].

III. RESULTS AND DISCUSSION

HAXPES survey spectra of the SrTiO_3 and TiO_2 single crystals show only the expected core and Auger lines of the oxides with no contaminants detectable (see Fig. S1 in the Supplemental Material [55]). In addition to the Ti core state and valence band spectra, which will be discussed in detail in the following, the O 1s for both samples as well as the Sr 2s, 2p_{3/2} and 3d core state spectra of SrTiO_3 were collected for completeness (see Fig. S2 in the Supplemental Material [55]). Figure 1(a) shows the Ti 1s and 2p HAXPES core level spectra of both crystals. The Ti 2p spectra show the 2p_{3/2} and 2p_{1/2} components with a SOS of 5.7 eV. The HAXPES and SXPS Ti 2p spectra are comparable (see Fig. S3 in the Supplemental Material [55]). In contrast, the Ti 1s does not exhibit SOS and therefore is advantageous for the identification of satellite features, as the overall spectral shape is simplified. In comparison with the 2s and 3s core levels, which also do not exhibit SOS, the 1s line has the lowest intrinsic linewidth (0.89 eV compared with 3.9 eV for 2s and 2.1 eV for 3s) [56], aiding the identification of low-energy satellite features.

Figure 1(b) shows an expanded view of the experimentally observed satellite features S_1 – S_7 with position guidelines based on the Ti 1s spectra for TiO_2 except for S_2 , which is only clearly observed in SrTiO_3 . The energy positions of the satellites are summarized in Table I. In the 2p spectra, satellite features appear twice due to SOS at a separation of 5.7 eV, e.g., S_3 at 13.4 and the spin-orbit split peak at 19.2 eV. While authors of a multitude of studies have reported on the satellites observed in the Ti 2p spectra, authors of only two previous studies report satellites in the Ti 1s spectra of SrTiO_3 and TiO_2 , noting satellite features at 5, 13, and 26 eV [20,57]. These values are in good agreement with the data presented

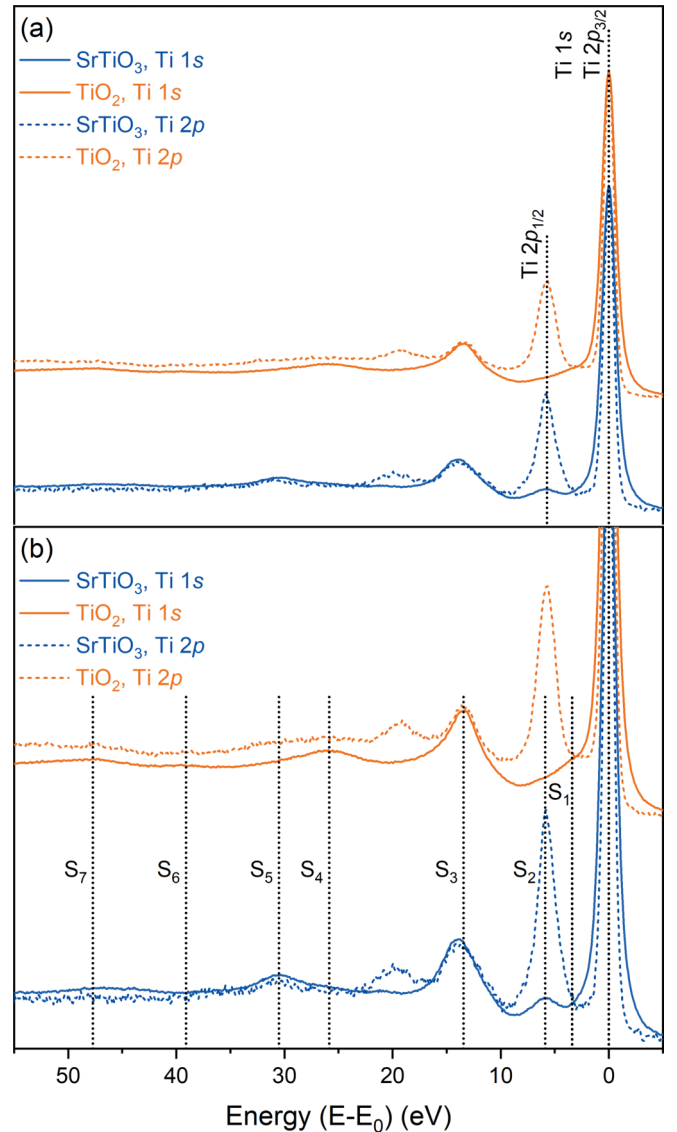


FIG. 1. Hard x-ray photoelectron spectroscopy (HAXPES) Ti 1s and 2p spectra of SrTiO_3 and TiO_2 , including (a) complete spectra and (b) magnified view of the satellite structure. All spectra are aligned to the main peak (1s and 2p_{3/2}) at 0 eV and a relative energy scale shown. The guidance lines in (b) are taken from the Ti 1s spectra at the satellite positions for TiO_2 except for S_2 , which is only clearly observed in SrTiO_3 .

here but do not include a discussion of the additional spectral features observed in this paper. Features S_4 and S_5 are associated with the Ti core level excitation, as will be discussed below.

TABLE I. Experimentally observed satellite positions relative to the main peaks (1s and 2p_{3/2}) at 0 eV. Features that cannot be clearly identified in the experimental data are denoted as not detectable (n.d.).

	S_1	S_2	S_3	S_4	S_5	S_6	S_7
TiO_2	3.4	5.7	13.4	25.9	30.5	39.1	47.7
SrTiO_3	n.d.	5.9	13.9	25.8	30.5	n.d.	46.6

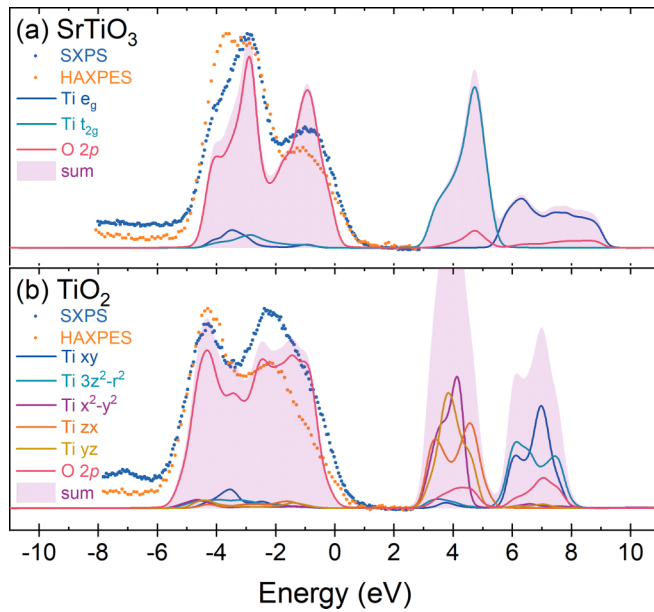


FIG. 2. Soft x-ray photoelectron spectroscopy (SXPS) and hard x-ray photoelectron spectroscopy (HAXPES) valence spectra and broadened, one-electron photo-ionization cross-section weighted local density approximation and dynamical mean-field theory (LDA+DMFT) projected density of states (PDOS) for (a) SrTiO₃ and (b) TiO₂. The sum of the individual PDOS contributions is also shown. The broadening and cross-section corrections were chosen to match the SXPS experimental setup. In the LDA+DMFT results, $\mu_{dc} = 3.0$ eV was used. Experimental data were aligned to the O $2p$ -dominated features at the bottom of the valence band.

Authors of previous cluster model studies for Ti $2p$ XPS of TiO₂ [39,52] explained that the two features (i) and (iii) at 0 and 13 eV correspond to bonding- and antibonding-split final states, respectively. The large energy splitting of the two final states is due to a strong Ti–O covalent bonding, i.e., a large hybridization between the $|d^0\rangle$ and charge-transferred $|d^1\bar{L}\rangle$ electronic configurations leads to a formation of well-defined bonding and antibonding states.

Before examining the multiple satellite features observed in the Ti $1s$ HAXPES spectra and discussing appropriate theoretical models of the core level excitations in the studied Ti compounds, the electronic structure calculations, which form the basis for the core level spectral calculations using LDA+DMFT AIM, are discussed. To validate the computational parameter, i.e., double-counting correction value μ_{dc} used in the LDA+DMFT self-consistent calculation, PDOS of both SrTiO₃ and TiO₂ are compared with SXPS and HAXPES valence spectra in Fig. 2. A good agreement in the overall shape and relative energy positions of features of the valence band states is found between theory and SXPS spectra. Practically, μ_{dc} renormalizes the energy levels of the metal $3d$ to the O $2p$ orbitals [32,49,58]. Thus, for a band insulator with a gap between empty metal $3d$ and filled O $2p$ bands, which is the case for SrTiO₃ and TiO₂, μ_{dc} can be estimated by reproducing the experimental bandgap. Here, $\mu_{dc} = 3.0$ eV yields good agreement to previously reported experimental bandgap (~ 3 eV) or inverse PES data [59,60]. The μ_{dc} determination

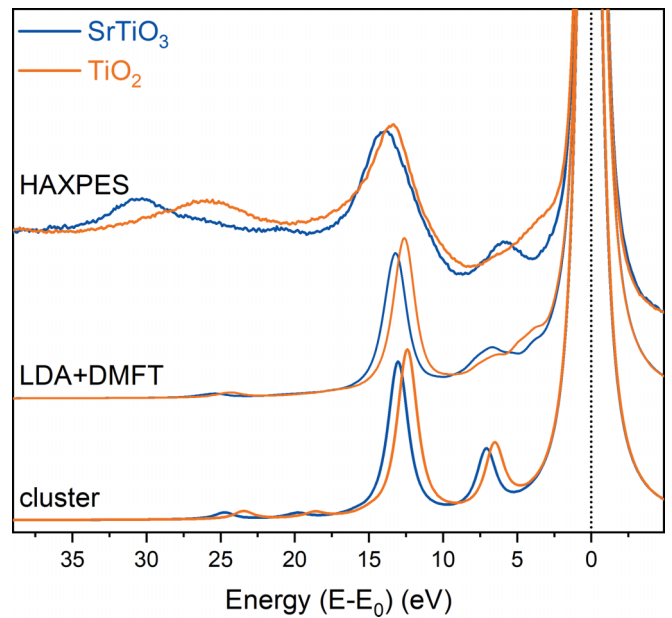


FIG. 3. Ti $1s$ spectra calculated by the cluster and local density approximation and dynamical mean-field theory (LDA+DMFT) Anderson impurity model (AIM) methods and from hard x-ray photoelectron spectroscopy (HAXPES) experiments for SrTiO₃ and TiO₂. All spectra are aligned to the $1s$ main peak at 0 eV, and a relative energy scale is shown.

can be found in Part B of the Supplemental Material (Figs. S4 and S5) [55].

The direct comparison of the theoretical PDOS with the HAXPES spectra illustrates the influence of the energy-dependent photo-ionization cross-sections. The relative increase in Ti s state cross-sections at higher x-ray photon energy leads to an increase in overall intensity at the bottom of the valence band. This ability to enhance s contributions represents another key advantage of HAXPES, which has been previously exploited to probe the valence band orbital character of other metal oxide systems [61–63]. As the Ti s and p as well as the O s states are not explicitly included in the LDA+DMFT calculations, the theory was corrected for the SXPS setup as, due to photo-ionization cross-section effects, the contributions from Ti d and O p states dominate at lower photon energies. The unbroadened, uncorrected theoretical PDOS results can be found in Fig. S6 in the Supplemental Material [55].

Building upon the electronic structure model, Ti $1s$ core level spectra were computed using the LDA+DMFT AIM for SrTiO₃ and TiO₂. Both experimental HAXPES and simulated Ti $1s$ spectra are shown in Fig. 3. The simulated spectra can reproduce the characteristic satellite features up to 30 eV above the main peak (including satellites S_1 – S_4 in the experimental spectra) in both compounds, with energy positions, relative intensities, and spectral shapes captured. The relative energy shift of the most intense feature S_3 is clear in both theory and experiment although theory underestimates the width of this feature. The low-energy satellites S_1 and S_2 are particularly well matched between experiment and theory for both TiO₂ and SrTiO₃, indicating that they are indeed intrinsic to the materials and have been missed in previous experiments focusing

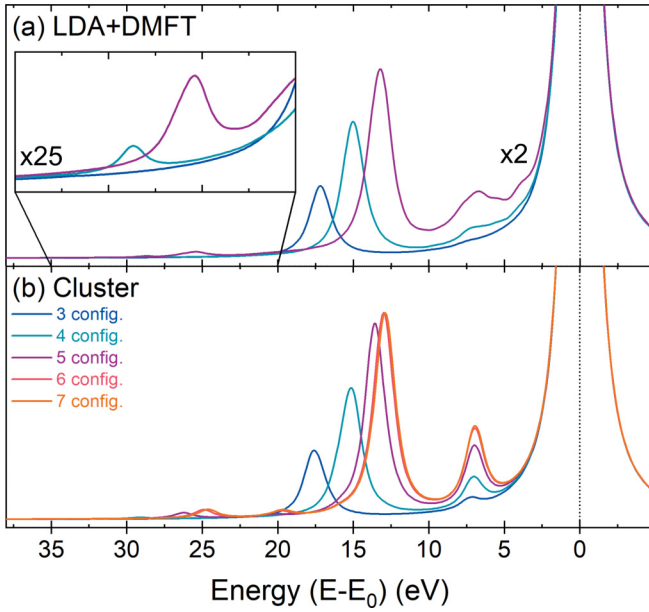


FIG. 4. SrTiO₃ Ti 1s hard x-ray photoelectron spectroscopy (HAXPES) spectra calculated by (a) local density approximation and dynamical mean-field theory (LDA+DMFT) Anderson impurity model (AIM) and (b) TiO₆ cluster model with varying number of electronic configurations (config.) included in the spectral simulation: three config. ($|d^0\rangle + |d^1\bar{L}\rangle + |d^2\bar{L}^2\rangle$), four config. ($|d^0\rangle + |d^1\bar{L}\rangle + |d^2\bar{L}^2\rangle + |d^3\bar{L}^3\rangle$), five config. ($|d^0\rangle + |d^1\bar{L}\rangle + |d^2\bar{L}^2\rangle + |d^3\bar{L}^3\rangle + |d^4\bar{L}^4\rangle$), six config. ($|d^0\rangle + |d^1\bar{L}\rangle + |d^2\bar{L}^2\rangle + |d^3\bar{L}^3\rangle + |d^4\bar{L}^4\rangle + |d^5\bar{L}^5\rangle$), and seven config. ($|d^0\rangle + |d^1\bar{L}\rangle + |d^2\bar{L}^2\rangle + |d^3\bar{L}^3\rangle + |d^4\bar{L}^4\rangle + |d^5\bar{L}^5\rangle + |d^6\bar{L}^6\rangle$). The inset in (a) shows a magnified view of the high-energy region of the spectra. All spectra are aligned to the main peak at 0 eV, and a relative energy scale is shown.

on Ti 2p spectra. Theory can also reproduce satellite S₄ at just below 26 eV in the experiment.

Given the good agreement between the theoretical calculations and the experimental data, the character of the spectral features can be identified based on further exploration of the theoretical parameters. Figure 4(a) shows the simulated Ti 1s spectra of SrTiO₃ calculated with varying number of electronic configurations included. Satellite S₃, and to a much subtler degree S₂, moves to lower energy relative to the main peak when higher configurations ($|d^2\bar{L}^2\rangle$, $|d^3\bar{L}^3\rangle$) are included. This behavior can be explained as the energies of these configurations with multiple electrons in the Ti 3d shell are rather high (>25 eV) due to the energy cost from the onsite *d-d* Coulomb repulsion, see Appendix B for the estimated values. However, the higher configurations are coupled to low-lying configurations ($|d^0\rangle$, $|d^1\bar{L}^1\rangle$) via the strong Ti–O covalent bonding, which renormalizes the entire spectrum, moving features S₃ and S₂ to lower energies. This indicates that, when implementing an impurity model analysis for core level PES of highly covalent TMOs, care must be taken regarding the number of electronic configurations included in the numerical simulation.

Figure 4 further explores a range of cluster model parameters and their validity for SrTiO₃. In the TiO₆ cluster model, the hopping parameter V on the nearest-neighbor Ti–O

bonds is taken from the tight-binding model constructed from the LDA bands. It gives estimates of $V_{e_g} = 4.01$ eV and $V_{t_{2g}} = -2.33$ eV for the Ti e_g and t_{2g} orbitals, respectively. These values are consistent with a previous DFT-based estimate by Haverkort *et al.* [64]. The parameter values of the present cluster model are summarized in Appendix B. The cluster model spectra including the basis configuration dependence, see Fig. 4(a), resemble the LDA+DMFT spectra in Fig. 4(b). Thus, the cluster model description works reasonably well for the Ti core level of SrTiO₃. However, the low-energy satellite features S₁ and S₂ in the cluster model are much sharper than in the LDA+DMFT AIM. This difference suggests that these satellites are related to the band structure since the LDA+DMFT description explicitly considers the O 2p bands, whereas only O 2p discrete levels on the nearest-neighbor ligands are included in the cluster model. The cluster model result also shows that the Ti 1s spectra are well converged by including up to five configurations in the basis expansion. In earlier studies using the cluster model implementing up to three configurations ($|d^0\rangle + |d^1\bar{L}\rangle + |d^2\bar{L}^2\rangle$) [39], the hopping parameter derived from a fitting analysis of experimental Ti 2p XPS data is ~25% smaller than the DFT-based estimate above. This suggests that the higher electronic configurations must be included in the fitting analysis of Ti core level spectra of Ti oxides.

The Ti 1s spectra computed by the isotropic cluster model, where $V_{e_g} = V_{t_{2g}} = 3.5$ eV and the crystal-field splitting (10Dq) is set to zero [see Fig. 5(a)], show satellite S₃ clearly, and its configuration dependence resembles the realistic cluster model in Fig. 4(b). However, the low-energy satellites S₁ and S₂ are not reproduced in the isotropic cluster model result. By switching the anisotropy in the hybridization on (i.e., $V_{e_g} \neq V_{t_{2g}}$), a satellite feature does appear albeit at a slightly higher energy of 7 eV than experiment and LDA+DMFT. It is worth noting that the satellite does not split from the satellite S₃. This behavior suggests that this satellite feature is related to a nonbonding state for the bonding state (main line) and the antibonding state forming satellite S₃. The simulation results allow modeling of the low-energy bonding properties of the studied Ti oxides by a very simple model provided in Appendix A. The crystal field splitting enhances the intensity of the low-energy satellite feature, as can be seen in Fig. 5(c). To emphasize the orbital character of the two satellites, Figs. 5(d)–5(f) show the cluster model spectra calculated with rescaled hopping parameters for e_g and t_{2g} orbitals. Here, the five-configuration basis expansion is employed in the spectral evaluation. The $V_{t_{2g}}$ hopping mainly modifies the binding energy of the low-energy satellite, whereas V_{e_g} hopping controls that of satellite S₃.

Finally, a clear material dependence in the satellite S₃ composed of the antibonding-split final states is observed. Since the bonding and antibonding splitting is determined largely by the hybridization on the nearest-neighbor Ti–O bond, the S₃ satellite of the cluster model is almost on top of the one in the LDA+DMFT AIM for both compounds, see Fig. 3. This is in clear contrast to satellite S₂, as discussed in Figs. 3 and 4. The S₃ satellite of TiO₂ is ~0.5 eV shallower than that of SrTiO₃, indicating a weaker Ti–O bonding in the former. This can be quantified by the effective hybridization strength V_{eff} that represents the coupling between the formal valence con-

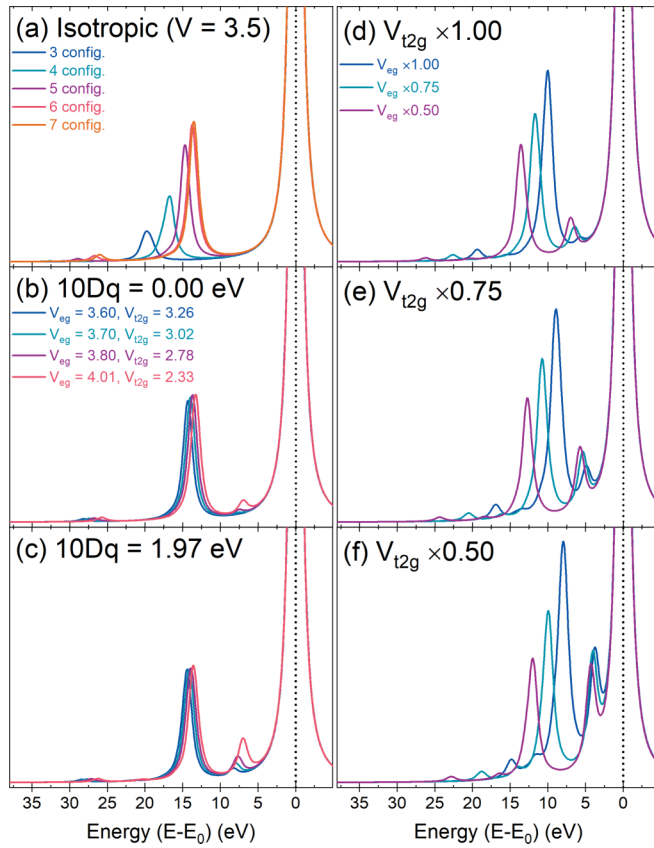


FIG. 5. Cluster model $1s$ spectra simulating SrTiO_3 . (a) Isotropic cluster model spectra computed with different configuration basis, see caption of Fig. 4 for details. (b)–(c) Cluster model spectra computed for selected hopping parameters with $10Dq = 0.00$ and 1.97 eV [the local density approximation (LDA) value], respectively. (d)–(f) Cluster model spectra computed by varying the V_{t2g} and V_{eg} values independently. The five-configuration basis is employed in (b)–(f). All spectra are aligned to the main peak at 0 eV, and a relative energy scale is shown.

figuration $|d^0\rangle$ and the charge-transferred one $|d^1\bar{L}\rangle$ [17,39]. The effective hybridization V_{eff} is defined as $\sqrt{4V_{eg}^2 + 6V_{t2g}^2}$ for SrTiO_3 and $\sqrt{2V_{B1g}^2 + 2V_{Ag}^2 + 2V_{Ag'}^2 + 2V_{B2g}^2 + 2V_{B3g}^2}$ for TiO_2 , which amounts to 9.84 and 9.49 eV, respectively, from the hopping amplitudes in the LDA result (see Appendix B). These estimates support a weaker Ti–O bonding in TiO_2 than in SrTiO_3 and emphasize a close relation between the satellite S_3 and the Ti–O bonding strength.

IV. CONCLUSIONS

PES is widely used to probe chemical environments and bonding as well as the electronic structure of TMOs. This paper showcases the usefulness of collecting deeper core level spectra in favor of the more commonly explored $2p$ states, using the example of Ti $1s$ spectra of SrTiO_3 and TiO_2 . The lack of SOS and favorable intrinsic linewidths lead to the observation of satellite features not observed previously. The presented theoretical approaches based on LDA+DMFT as well as a conventional cluster model

provide a good description of the experimental spectra. The comparison emphasizes the crucial importance of explicitly including higher-order Ti–O charge-transfer processes beyond the nearest-neighboring Ti–O bonds. Finally, this paper confirms that the presented theoretical approaches can provide a successful description of early TMOs, where covalency plays a central role, promising wider applicability to the many technologically crucial materials in this family of compounds.

ACKNOWLEDGMENTS

A.H. was supported by JSPS KAKENHI Grants No. 21K13884 and No. 21H01003. C.K. acknowledges the support from the Department of Chemistry, UCL. A.R. acknowledges the support from the Analytical Chemistry Trust Fund for her CAMS-UK Fellowship and from Imperial College London for her Imperial College Research Fellowship. The authors would like to thank T. Uozumi for valued discussions.

APPENDIX A: TOY MODEL FOR THE LOW-ENERGY SATELLITES

Here, a simple toy model for the low-energy satellites in Fig. 5 is proposed. The model consists of three levels labeled as $|0\rangle$, $|e\rangle$, and $|t\rangle$. Here, $|0\rangle$ represents an ionic tetravalent Ti state, i.e., it corresponds to the $|d^0\rangle$ configuration in the AIM or cluster model description. Also, $|e\rangle$ ($|t\rangle$) simulate states with an e_g (t_{2g}) Ti $3d$ electron and a hole on ligands in the $|d^1\bar{L}\rangle$ configuration. Considering the matrix elements by the charge transfer between the Ti site and ligands, the low-energy excitations of the studied Ti compounds can be modeled by the 3×3 Hamiltonian with the basis order $\{|0\rangle, |e\rangle, |t\rangle\}$:

$$H = \begin{pmatrix} 0 & t_e & t_t \\ t_e & e_e & 0 \\ t_t & 0 & e_t \end{pmatrix},$$

where e_e (and e_t) account for the charge-transfer energy and the crystal field splitting; thus, $e_e \neq e_t$ in reality. The v_e and v_t are the hopping amplitude for the e_g and t_{2g} orbitals with the ligand orbitals, respectively. Next, by applying the hopping term in the Hamiltonian to the $|0\rangle$ state, a state $|b\rangle$, and then an orthogonal state $|n\rangle$ are obtained as

$$|b\rangle = \frac{1}{\sqrt{t_e^2 + t_t^2}}(t_e|e\rangle + t_t|t\rangle),$$

and

$$|n\rangle = \frac{1}{\sqrt{t_e^2 + t_t^2}}(t_t|e\rangle - t_e|t\rangle).$$

Representing the Hamiltonian with the $\{|0\rangle, |b\rangle, |n\rangle\}$ basis set,

$$H = \begin{pmatrix} 0 & \sqrt{t_e^2 + t_t^2} & 0 \\ \sqrt{t_e^2 + t_t^2} & \frac{e_e t_e^2 + e_t t_t^2}{t_e^2 + t_t^2} & \frac{(e_e - e_t)t_e t_t}{t_e^2 + t_t^2} \\ 0 & \frac{(e_e - e_t)t_e t_t}{t_e^2 + t_t^2} & \frac{e_e t_e^2 + e_t t_t^2}{t_e^2 + t_t^2} \end{pmatrix}.$$

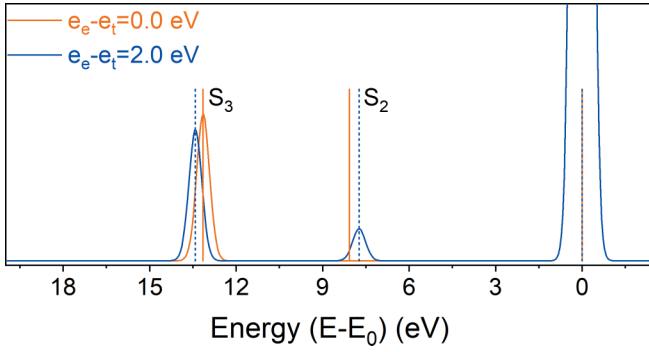


FIG. 6. The simulated x-ray photoelectron spectroscopy (XPS) spectra of the toy model. (red) The spectrum with $e_e = e_t$, i.e., the crystal field splitting is zero. (blue) The spectrum with $e_e - e_t = 1.97$ eV. The vertical lines indicate the energies of the final states in the toy model for the two cases. When $e_e = e_t$, the nonbonding state is present at the energy of 8.07 eV, but its spectral intensity is zero.

By the above construction, the $|0\rangle$ and $|n\rangle$ states do not couple. Note that modeling the $1s$ XPS final states shifts the energies e_e and e_t by the core-hole potential U_{dc} due to the presence of the $1s$ core hole; thus, the structure of the Hamiltonian above does not change.

When $e_e = e_t \equiv e$, i.e., the crystal field splitting is zero, the nonbonding state $|n\rangle$ is fully decoupled from the $|0\rangle$ and $|b\rangle$ states, and the Hamiltonian becomes

$$H = \begin{pmatrix} 0 & \sqrt{t_e^2 + t_t^2} & 0 \\ \sqrt{t_e^2 + t_t^2} & \frac{et_e^2 + et_t^2}{t_e^2 + t_t^2} & 0 \\ 0 & 0 & \frac{et_t^2 + et_e^2}{t_e^2 + t_t^2} \end{pmatrix}.$$

In this limit, the $1s$ spectrum is composed of two states: the bonding and antibonding states (of the $|0\rangle$ and $|b\rangle$ states), which produce the 0 and 13 eV (S_3) peaks in the experimental data, respectively. When $e_e \neq e_t$ in the realistic case with the crystal field splitting, the contribution of the nonbonding state $|n\rangle$ shows up in the spectrum in between the two peaks, yielding the S_2 satellite. Since the coupling of the $|b\rangle$ and $|n\rangle$ states is in general very weak compared with the hybridization strength between the $|b\rangle$ and $|0\rangle$ states ($= \sqrt{t_e^2 + t_t^2}$), it can be viewed as a weak perturbation to the bonding and antibonding formation of the Ti–O network. Thus, it does not yield a large peak shift nor intensity modulation to the two peaks, as observed in Fig. 5.

Figure 6 shows the XPS spectra computed from the toy model. To simulate the studied Ti oxides, model parameters are extracted from the cluster model studied above

TABLE II. The parameter values adopted in the TiO_6 cluster model for simulating SrTiO_3 in electronvolts.

U_{dd}	U_{cd}	V_{e_g}	$V_{t_{2g}}$	$10Dq$
4.50	5.40	4.01	-2.33	1.97

TABLE III. The hopping parameter values adopted in the TiO_6 cluster model for simulating TiO_2 in electronvolts.

$V_{B_{1g}}$	V_{A_g}	$V_{A'_g}$	$V_{B_{2g}}$	$V_{B_{3g}}$
3.87	3.85	-2.35	-2.15	-2.25

as $v_e = r\sqrt{4V_{e_g}^2}$, $v_t = r\sqrt{6V_{t_{2g}}^2}$, $e_e = \Delta_{CT} + 6Dq$, and $e_t = \Delta_{CT} - 4Dq$, where $V_{e_g} = 4.01$ eV, $V_{t_{2g}} = -2.33$ eV, charge-transfer energy $\Delta_{CT} = 3.00$ eV, and the crystal field splitting $10Dq = 1.97$ eV. To consider the effect of the higher-order Ti–O charge-transfer processes, the hopping parameter values are rescaled by a constant factor $r = 0.65$. The toy model reproduces the spectra of the cluster model with many-body electronic configurations in Fig. 5 nicely. The vertical lines indicate the eigenstate energies of the final state Hamiltonian. When the crystal field splitting is absent, the nonbonding state is present between 0 eV and S_3 peaks but not visible in the spectrum. With the finite crystal field splitting, the nonbonding state appears at ~ 7 eV with a smaller spectral intensity than the other two peaks.

It is worth noting that, in the cluster model result of Fig. 5(b), the nonbonding satellite S_2 has a nonzero spectral intensity even when $10Dq = 0.00$ eV unless the hopping parameter for the Ti e_g and t_{2g} orbitals is isotropic ($V_{e_g} = V_{t_{2g}}$). However, the visibility of the S_2 satellite in the toy model seems to concern only the presence of the crystal field splitting. This is an artifact of this simple toy model. The S_2 satellite gets a finite intensity for $V_{e_g} \neq V_{t_{2g}}$ by including higher-order states with two Ti d electrons (and two ligand holes) to the toy model above. Only when fully isotropic ($10Dq$ is zero and $V_{e_g} = V_{t_{2g}}$), see Fig. 5(a), the nonbonding satellite S_2 cannot be excited in the XPS process.

APPENDIX B: PARAMETERS OF THE TiO_6 CLUSTER MODEL

The parameters defining the cluster model of SrTiO_3 are summarized in Table II. The electron hopping amplitude V_{e_g} ($V_{t_{2g}}$) of the Ti e_g (t_{2g}) orbital with the nearest-neighboring molecular orbital of the ligands and the crystal field splitting $10Dq$ are read from the tight-binding model constructed from the LDA bands. The interaction parameters U_{dd} , U_{cd} are set to the same values as in the LDA+DMFT AIM. The charge-transfer energy Δ_{CT} is set to 3.0 eV. The Ti $1s$ core level spectra are rather insensitive to the Δ_{CT} value in

TABLE IV. The configuration diagonal energies in the TiO_6 cluster model for SrTiO_3 and TiO_2 in electronvolts.

$ d^0\rangle$	0	0.0
$ d^1\bar{L}^1\rangle$	Δ	3.0
$ d^2\bar{L}^2\rangle$	$2\Delta + U_{dd}$	10.5
$ d^3\bar{L}^3\rangle$	$3\Delta + 3U_{dd}$	22.5
$ d^4\bar{L}^4\rangle$	$4\Delta + 6U_{dd}$	39.0
$ d^5\bar{L}^5\rangle$	$5\Delta + 10U_{dd}$	60.0
$ d^6\bar{L}^6\rangle$	$6\Delta + 15U_{dd}$	85.5

a realistic range. Table III shows the hopping amplitude of different orbitals [$B_{1g}(xy)$, $A_g(3z^2 - r^2)$, $A'_g(x^2 - y^2)$, $B_{2g}(zx)$, and $B_{3g}(yz)$] in TiO_2 .

Table IV summarizes the configuration diagonal energies accounting for the interaction U_{dd} and the charge-transfer energy Δ_{CT} up to $|d^6\bar{L}^6\rangle$ configurations.

-
- [1] M. Imada, A. Fujimori, and Y. Tokura, *Rev. Mod. Phys.* **70**, 1039 (1998).
- [2] D. I. Khomskii, *Transition Metal Compounds* (Cambridge University Press, Cambridge, 2014).
- [3] F. Borgatti, P. Torelli, and G. Panaccione, *J. Electron Spectrosc. Relat. Phenom.* **208**, 95 (2016).
- [4] C. Kalha, N. K. Fernando, P. Bhatt, F. O. L. Johansson, A. Lindblad, H. Rensmo, L. Z. Medina, R. Lindblad, S. Siol, L. P. H. Jeurgens *et al.*, *J. Phys.: Condens. Matter* **33**, 233001 (2021).
- [5] S. Tanuma, C. J. Powell, and D. R. Penn, *Surf. Interface Anal.* **21**, 165 (1994).
- [6] K. Horiba, M. Taguchi, A. Chainani, Y. Takata, E. Ikenaga, D. Miwa, Y. Nishino, K. Tamasaku, M. Awaji, A. Takeuchi *et al.*, *Phys. Rev. Lett.* **93**, 236401 (2004).
- [7] M. van Veenendaal, *Phys. Rev. B* **74**, 085118 (2006).
- [8] A. Hariki, T. Uozumi, and J. Kuneš, *Phys. Rev. B* **96**, 045111 (2017).
- [9] M. Taguchi, M. Matsunami, Y. Ishida, R. Eguchi, A. Chainani, Y. Takata, M. Yabashi, K. Tamasaku, Y. Nishino, T. Ishikawa *et al.*, *Phys. Rev. Lett.* **100**, 206401 (2008).
- [10] R. Eguchi, M. Taguchi, M. Matsunami, K. Horiba, K. Yamamoto, Y. Ishida, A. Chainani, Y. Takata, M. Yabashi, D. Miwa *et al.*, *Phys. Rev. B* **78**, 075115 (2008).
- [11] M. Obara, A. Sekiyama, S. Imada, J. Yamaguchi, T. Miyamachi, T. Balashov, W. Wulfhekel, M. Yabashi, K. Tamasaku, A. Higashiya *et al.*, *Phys. Rev. B* **81**, 113107 (2010).
- [12] N. Kamakura, M. Taguchi, A. Chainani, Y. Takata, K. Horiba, K. Yamamoto, K. Tamasaku, Y. Nishino, D. Miwa, E. Ikenaga *et al.*, *Europhys. Lett.* **68**, 557 (2004).
- [13] A. Hariki, Y. Ichinozuka, and T. Uozumi, *J. Phys. Soc. Jpn.* **82**, 043710 (2013).
- [14] M. Taguchi, A. Chainani, N. Kamakura, K. Horiba, Y. Takata, M. Yabashi, K. Tamasaku, Y. Nishino, D. Miwa, T. Ishikawa *et al.*, *Phys. Rev. B* **71**, 155102 (2005).
- [15] C. F. Chang, T. C. Koethe, Z. Hu, J. Weinen, S. Agrestini, L. Zhao, J. Gegner, H. Ott, G. Panaccione, H. Wu *et al.*, *Phys. Rev. X* **8**, 021004 (2018).
- [16] M. A. van Veenendaal and G. A. Sawatzky, *Phys. Rev. Lett.* **70**, 2459 (1993).
- [17] M. Ghiasi, A. Hariki, M. Winder, J. Kuneš, A. Regoutz, T.-L. Lee, Y. Hu, J.-P. Rueff, and F. M. F. de Groot, *Phys. Rev. B* **100**, 075146 (2019).
- [18] P. Miedema, F. Borgatti, F. Offi, G. Panaccione, and F. de Groot, *J. Electron Spectrosc. Relat. Phenom.* **203**, 8 (2015).
- [19] B. T. Young, D. R. Heskett, C. Cuong Nguyen, M. Nie, J. C. Woicik, and B. L. Lucht, *ACS Appl. Mater. Interfaces* **7**, 20004 (2015).
- [20] J. C. Woicik, C. Weiland, and A. K. Rumaiz, *Phys. Rev. B* **91**, 201412(R) (2015).
- [21] J. Rubio-Zuazo, A. Chainani, M. Taguchi, D. Malterre, A. Serrano, and G. R. Castro, *Phys. Rev. B* **97**, 235148 (2018).
- [22] J. Berens, S. Bichelmaier, N. K. Fernando, P. K. Thakur, T.-L. Lee, M. Mascheck, T. Wiell, S. K. Eriksson, J. M. Kahk, J. Lischner *et al.*, *J. Phys.: Energy* **2**, 035001 (2020).
- [23] S. Siol, J. Mann, J. Newman, T. Miyayama, K. Watanabe, P. Schmutz, C. Cancellieri, and L. P. Jeurgens, *Surf. Interface Anal.* **52**, 802 (2020).
- [24] C. Kalha, L. E. Ratcliff, J. J. Gutiérrez Moreno, S. Mohr, M. Mantsinen, N. K. Fernando, P. K. Thakur, T.-L. Lee, H.-H. Tseng, T. S. Nunney *et al.*, *Phys. Rev. B* **105**, 045129 (2022).
- [25] M. Calandra, J. P. Rueff, C. Gougoussis, D. Céolin, M. Gorgoi, S. Benedetti, P. Torelli, A. Shukla, D. Chandesris, and C. Brouder, *Phys. Rev. B* **86**, 165102 (2012).
- [26] J. Thien, J. Bahlmann, A. Alexander, M. Hoppe, T. Pohlmann, K. Ruwisch, C. Meyer, F. Bertram, K. Küpper, and J. Wollschläger, *J. Phys. Chem. C* **124**, 23895 (2020).
- [27] F. de Groot and A. Kotani, *Core Level Spectroscopy of Solids* (CRC Press, Boca Raton, 2014).
- [28] A. E. Bocquet, T. Mizokawa, T. Saitoh, H. Namatame, and A. Fujimori, *Phys. Rev. B* **46**, 3771 (1992).
- [29] G. Kotliar, S. Y. Savrasov, K. Haule, V. S. Oudovenko, O. Parcollet, and C. A. Marianetti, *Rev. Mod. Phys.* **78**, 865 (2006).
- [30] A. Georges, G. Kotliar, W. Krauth, and M. J. Rozenberg, *Rev. Mod. Phys.* **68**, 13 (1996).
- [31] A. Hariki, A. Yamanaka, and T. Uozumi, *Europhys. Lett.* **114**, 27003 (2016).
- [32] K. Higashi, M. Winder, J. Kuneš, and A. Hariki, *Phys. Rev. X* **11**, 041009 (2021).
- [33] A. Regoutz, M. Mascheck, T. Wiell, S. K. Eriksson, C. Liljenberg, K. Tetzner, B. A. D. Williamson, D. O. Scanlon, and P. Palmgren, *Rev. Sci. Instrum.* **89**, 073105 (2018).
- [34] T. Hashimoto, P. Amann, A. Regoutz, N. Barrett, L. F. J. Piper, W. Hamouda, O. Renault, M. Lundwall, and M. Machida, *Vacuum Surf. Sci.* **64**, 493 (2021).
- [35] J. Kuneš, I. Leonov, M. Kollar, K. Byczuk, V. I. Anisimov, and D. Vollhardt, *Eur. Phys. J.: Spec. Top.* **180**, 5 (2009).
- [36] P. Blaha, K. Schwarz, G. K. H. Madsen, D. Kvasnicka, J. Luitz, R. Laskowski, F. Tran, and L. D. Marks *WIEN2k, An Augmented Plane Wave + Local Orbitals Program for Calculating Crystal Properties* (Vienna University of Technology, Vienna, 2018).
- [37] J. Kuneš, R. Arita, P. Wissgott, A. Toschi, H. Ikeda, and K. Held, *Comput. Phys. Commun.* **181**, 1888 (2010).
- [38] A. A. Mostofi, J. R. Yates, G. Pizzi, Y.-S. Lee, I. Souza, D. Vanderbilt, and N. Marzari, *Comput. Phys. Commun.* **185**, 2309 (2014).
- [39] K. Okada, T. Uozumi, and A. Kotani, *J. Phys. Soc. Jpn.* **63**, 3176 (1994).
- [40] A. Tanaka and T. Jo, *J. Phys. Soc. Jpn.* **63**, 2788 (1994).
- [41] A. E. Bocquet, T. Mizokawa, K. Morikawa, A. Fujimori, S. R. Barman, K. Maiti, D. D. Sarma, Y. Tokura, and M. Onoda, *Phys. Rev. B* **53**, 1161 (1996).
- [42] F. Lechermann, W. Heckel, O. Kristanovski, and S. Müller, *Phys. Rev. B* **95**, 195159 (2017).

- [43] E. Pavarini, S. Biermann, A. Poteryaev, A. I. Lichtenstein, A. Georges, and O. K. Andersen, *Phys. Rev. Lett.* **92**, 176403 (2004).
- [44] S. Okamoto, A. J. Millis, and N. A. Spaldin, *Phys. Rev. Lett.* **97**, 056802 (2006).
- [45] P. Werner, A. Comanac, L. de' Medici, M. Troyer, and A. J. Millis, *Phys. Rev. Lett.* **97**, 076405 (2006).
- [46] L. Boehnke, H. Hafermann, M. Ferrero, F. Lechermann, and O. Parcollet, *Phys. Rev. B* **84**, 075145 (2011).
- [47] H. Hafermann, K. R. Patton, and P. Werner, *Phys. Rev. B* **85**, 205106 (2012).
- [48] A. Hariki, A. Yamanaka, and T. Uozumi, *J. Phys. Soc. Jpn.* **84**, 073706 (2015).
- [49] M. Karolak, G. Ulm, T. Wehling, V. Mazurenko, A. Poteryaev, and A. Lichtenstein, *J. Electron Spectrosc. Relat. Phenom.* **181**, 11 (2010).
- [50] M. Jarrell and J. Gubernatis, *Phys. Rep.* **269**, 133 (1996).
- [51] M. Winder, A. Hariki, and J. Kuneš, *Phys. Rev. B* **102**, 085155 (2020).
- [52] K. Okada and A. Kotani, *J. Electron Spectrosc. Relat. Phenom.* **62**, 131 (1993).
- [53] J. Scofield, *J. Electron Spectrosc. Relat. Phenom.* **8**, 129 (1976).
- [54] C. Kalha, N. Fernando, and A. Regoutz, Digitisation of Scofield Photoionisation Cross Section Tabulated Data. *figshare. Dataset* (2020).
- [55] See Supplemental Material at <http://link.aps.org/supplemental/10.1103/PhysRevB.106.205138> for additional SXPS and HAX-PES spectra as well as details of the double-counting dependence of LDA+DMFT.
- [56] J. Campbell and T. Papp, *At. Data Nucl. Data Tables* **77**, 1 (2001).
- [57] N. Moslemzadeh, G. Beamson, P. Tsakirooulos, J. Watts, S. Haines, and P. Weightman, *J. Electron Spectrosc. Relat. Phenom.* **152**, 148 (2006).
- [58] K. Haule, *Phys. Rev. Lett.* **115**, 196403 (2015).
- [59] Y. Tezuka, S. Shin, T. Ishii, T. Ejima, S. Suzuki, and S. Sato, *J. Phys. Soc. Jpn.* **63**, 347 (1994).
- [60] A. Ohtomo and H. Y. Hwang, *Nature (London)* **427**, 423 (2004).
- [61] D. J. Payne, R. G. Egdell, G. Paolicelli, F. Offi, G. Panaccione, P. Lacovig, G. Monaco, G. Vanko, A. Walsh, G. W. Watson *et al.*, *Phys. Rev. B* **75**, 153102 (2007).
- [62] J. J. Mudd, T.-L. Lee, V. Muñoz Sanjosé, J. Zúñiga-Pérez, D. J. Payne, R. G. Egdell, and C. F. McConville, *Phys. Rev. B* **89**, 165305 (2014).
- [63] D. Takegami, L. Nicolai, T. C. Koethe, D. Kasinathan, C. Y. Kuo, Y. F. Liao, K. D. Tsuei, G. Panaccione, F. Offi, G. Monaco *et al.*, *Phys. Rev. B* **99**, 165101 (2019).
- [64] M. W. Haverkort, M. Zwierzycki, and O. K. Andersen, *Phys. Rev. B* **85**, 165113 (2012).